Journal of ELECTRONIC MATERIALS, Vol. 48, No. 7, 2019
https://doi.org/10.1007/s11664-019-07179-6

Structural, Optical, and Magnetic Properties of Co-Doped SnO_2 Nanoparticles

M. YEHIA ,[1,3] SH. LABIB,[2] and S.M. ISMAIL[1]

1.—Reactor Physics Department, Nuclear Researches Center, Atomic Energy Authority, P.O. Box 13759, Cairo, Egypt. 2.—Nuclear Chemistry Department, Hot Laboratories Center, Atomic Energy Authority, P.O. Box 13759, Cairo, Egypt. 3.—e-mail: m6yehia@yahoo.com

Cobalt-doped SnO_2 nanoparticles with different cobalt concentrations have been prepared using a polyol method, and x-ray diffraction (XRD) analysis and Fourier-transform infrared spectroscopy applied to investigate their structure. The XRD patterns of all the prepared nanoparticles revealed single-phase tetragonal structure. The morphology of the nanoparticles was studied using scanning electron microscopy. Ultraviolet–visible absorbance spectroscopy measurements were utilized to understand the optical properties, revealing the dependence of the bandgap on the cobalt doping concentration. Magnetic measurements revealed that the samples exhibited room-temperature ferromagnetism, which should be an intrinsic characteristic. The origin of the room-temperature ferromagnetism was investigated using vibrating-sample magnetometry and electron spin resonance spectroscopy.

Key words: Diluted magnetic semiconductors, SnO_2, optical properties, bound magnetic polaron, electron spin resonance

INTRODUCTION

Tin oxide (SnO_2) is an *n*-type, wide-bandgap (3.6 eV) semiconductor oxide with O=Sn=O structure. It is a very promising material because of its optical transparency, high chemical stability, high sensitivity to various toxic gases, and compatibility with microfabrication processes. Its superior optical transparency makes it suitable for an impressive range of applications, e.g. in solar cells, as a catalytic support material, in solid-state chemical sensors, etc.[1] Simultaneously, since the prediction of room-temperature ferromagnetism (RTFM) in Mn-doped ZnO,[2,3] such oxide semiconductors have been extensively researched as possible dilute magnetic semiconductors. Defects play a key role in the chemical and physical properties of semiconducting materials. Lattice imperfections due to oxygen vacancies and structural defects in metal oxides can modify the bandgap, enhance the room-temperature ferromagnetism, and increase their range of applications.[4–6] In this case, oxygen vacancies can be considered as a kind of self-doping which does not change the intrinsic structure of SnO_2 crystal but modifies the bandgap energy, dielectric properties, and room-temperature ferromagnetism. Recent reports on doping of SnO_2 in bulk and nanoparticle form with magnetic transition metals (TMs) have revealed considerable ferromagnetism at and above room temperature. The possibility of such room- and high-temperature ferromagnetism in magnetic TM-doped SnO_2 systems has received a lot of attention in the field of diluted magnetic semiconductors (DMS) due to its applications in spintronic devices.[7] However, the exact mechanism inducing magnetism in doped SnO_2 nanoparticles is not yet fully understood. Various mechanisms have been suggested to explain the ferromagnetism of DMS, including the double-exchange interaction, bound magnetic polarons, and vacancies in the structure.[4,8] Various metal ions have been used as dopants of SnO_2, including Fe^{3+},[9,10] Ce^{3+},[11] Mn^{2+},[11] Co^{2+},[12,13] Ni^{2+},[14] and Cr^{3+}.[15] Such studies have provided interesting information about the

(Received December 10, 2018; accepted March 28, 2019; published online April 9, 2019)

relationships between doping, defect-related luminescence, surface effects, changes in morphology, particle size, and RTFM.[16]

In this work, single-phase $Sn_{1-x}Co_xO_2$ nanoparticles were prepared using a polyol method, a green nanotechnology alternative that offers the advantages of simplicity, low cost, and relatively low reaction temperature. The structural and morphological characteristics were studied using x-ray powder diffraction (XRD) analysis, Fourier-transform infrared (FTIR) spectroscopy, and scanning electron microscopy (SEM). Ultraviolet–visible (UV–Vis) spectroscopy measurements were utilized to understand the optical properties and the dependence of the bandgap energy on the cobalt concentration. Both vibrating-sample magnetometry (VSM) and electron spin resonance (ESR) spectroscopy were applied to explore the magnetic properties of the prepared nanoparticles.

EXPERIMENTAL PROCEDURES

Materials and Methods

Nano $Sn_{1-x}Co_xO_2$ (x = 0, 0.001, 0.005, 0.05, 0.1) powders were prepared using stannic chloride ($SnCl_4{\cdot}5H_2O$, 97.5%; Adwic Laboratory Chemicals, Egypt), $CoCl_2{\cdot}6H_2O$, glycerol ($C_3H_8O_3$, 99.5%; Genchem, China). The solutions were prepared using deionized water (18.2 MΩ) from a Millipore water purification system. Different nanoparticle samples were prepared using a simple green route derived from the sol–gel method given in Ref. 17 with slight modification. Pure SnO_2 was prepared by dissolving 1 mol $SnCl_4{\cdot}5H_2O$ in an appropriate amount of glycerol dissolved in 20 ml dis. H_2O. Co-doped $Sn_{1-x}Co_xO_2$ (x = 0.001, 0.005, 0.05, 0.01) was prepared by dissolving $SnCl_4{\cdot}5H_2O$ and $CoCl_2{\cdot}6H_2O$ in glycerol solution. Viscous gels formed, and complete dissolution of the added precursors was achieved by stirring on a hot plate at 80°C. The dissolved gels were kept on the hot plate until complete evaporation of the aqueous solution and ignition of the precursors occurred. The obtained ash was dried at 200°C for 2 h using a heating rate of 10°C/min. Finally, the dried powders were thermally treated at 500°C for 4 h using a heating rate of 10°C/min.

Characterization

The structure of the prepared samples was studied at room temperature using x-ray diffraction (XRD) analysis (Philips X'Pert multipurpose diffractometer) with Cu K_α radiation (with λ = 1.5418 Å). The crystal structure was refined by the Rietveld profile method using Rex software.[18] Microstructural investigations of the different powders were carried out using scanning electron microscopy (SEM, JSM-6510 LA; JEOL, Japan) in high vacuum using an accelerating voltage of 20 kV, working distance of 11 mm, and magnification of ×2000. Fourier-transform infrared (FTIR) spectroscopy (Nicolet iS10 FTIR Spectrometer; Thermo Scientific) was carried out on the prepared powders using the KBr disc technique, scanning in the region of 400 cm^{-1} to 1000 cm^{-1}. Optical studies were performed by ultraviolet–visible (UV–Vis) absorbance spectroscopy (Unicam, UK), using distilled water (18 MΩ) as reference, with analysis at different wavelengths ranging from 300 nm to 500 nm.

Magnetic measurements on the synthesized nanoparticles were carried out using vibrating-sample magnetometry (VSM, 9600-1 LDJ, USA) with a maximum applied field of nearly 20 kG at room temperature to determine the saturation magnetization M_s and coercivity H_c. Electron spin resonance (ESR) measurements were carried out at frequency of υ = 9.71 GHz using a standard X-band Bruker EMX spectrometer.

RESULTS AND DISCUSSION

Structural Characterization and Morphology

X-ray diffraction patterns of the $Sn_{1-x}Co_xO_2$ samples are shown in Fig. 1. All diffraction peaks coincide with those of the tetragonal rutile SnO_2 structure. No remarkable shift in the diffraction peaks or peaks from other phases were detected, revealing that the SnO_2 samples were of high purity. Rietveld refinement using Rex software was applied to determine the lattice parameters a and c and particle size (Table I). Both a and c were

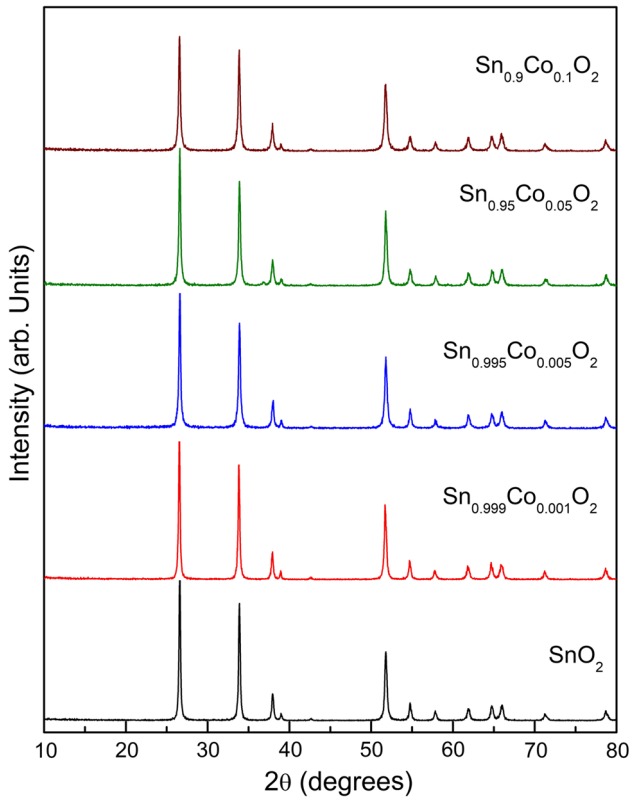

Fig. 1. X-ray diffraction patterns of different $Sn_{1-x}Co_xO_2$ nanoparticles.

almost constant, showing a minor dependence on the Co content x. This behavior again suggests that all the prepared samples comprised a single phase with high purity. The particle sizes (D) varied for the different Co-doped samples, ranging from 49 nm to 64 nm.

Figure 2 shows SEM images of $Sn_{1-x}Co_xO_2$ thermally treated at 500°C for 4 h. As shown in these images, a clear variation in the morphology was observed for the different Co-doped samples. SnO_2 consisted of peels containing spherical agglomerated particles under the surface. The SEM image of $Sn_{0.999}Co_{0.001}O_2$ showed a transformation of the peeling surface to a hierarchical monolithic structure in which spheres are embedded in three dimensions (3D). On the other hand, the $Sn_{0.995}Co_{0.005}O_2$ sample was characterized by the presence of a densified structure with round crystal grains deposited over a very smooth thin-film-like structure. The $Sn_{0.95}Co_{0.05}O_2$ sample consisted of nanohierarchical layered structures. The $Sn_{0.9}Co_{0.1}O_2$ sample consisted of flakes containing 3D spheres. Such differences in SEM images have been reported before for Co-doped SnO_2.[19] The change in morphology with increasing Co content may be caused by the change in lattice energy[20] as well as the variation of the defect concentrations, as mentioned below. The development from nanoflakes to nanohierarchical to layered thin-film structure is important, forming channels for electron transport in the SnO_2 crystals.[21]

To understand the structural evolution of the prepared nanopowders, FTIR spectra of $Sn_{1-x}Co_xO_2$ powders are shown in Fig. 3. The analysis focuses on the region from 1000 cm^{-1} to 400 cm^{-1}. Generally, the bands detected in the range from 400 cm^{-1} to 570 cm^{-1} are due to Sn–O stretching modes.[22] The FTIR spectrum of SnO_2 showed a band at 612 cm^{-1}, which can be assigned to the Sn–O fundamental vibration.[17] The shoulder appearing at 465 cm^{-1} can be attributed to Sn–O–Sn symmetric stretching modes. The small shoulder appearing at 417 cm^{-1} is due to Sn–O stretching modes.[22–24] The $Sn_{0.999}Co_{0.001}O_2$ and $Sn_{0.99}Co_{0.01}O_2$ samples were characterized by the presence of the same fundamental bands as observed for the pure sample. In addition, the development of small shoulders at 661 cm^{-1} and 668 cm^{-1} can be attributed to Sn–O–Sn antisymmetric stretching modes.[19] More bands and shoulders were observed for the $Sn_{0.995}Co_{0.005}O_2$ and $Sn_{0.95}Co_{0.05}O_2$ samples, corresponding to both symmetric and antisymmetric Sn–O–Sn modes as outlined above. The presence of these bands and shoulders is due to structural distortions in SnO_2 caused by surface defects and oxygen vacancies.[23] The variation of the bands and shoulders can be related not only to the concentration of Co^{2+} in the SnO_2 lattice structure but also to

Table I. Lattice parameters a and c, c/a ratio, and average particle size D (nm)

Sample	a (Å)	c (Å)	c/a	D (nm)
0	4.74	3.19	0.67	58
0.001	4.76	3.20	0.67	64
0.005	4.76	3.20	0.67	49
0.05	4.79	3.22	0.67	55
0.1	4.78	3.21	0.67	49

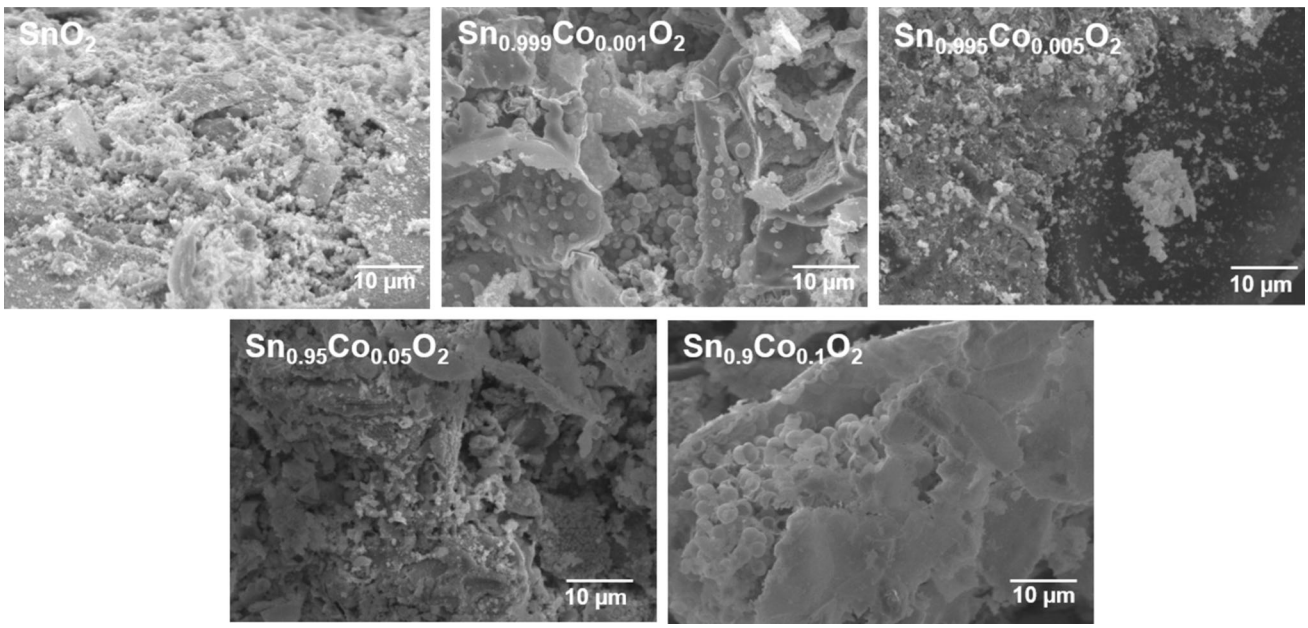

Fig. 2. SEM images of $Sn_{1-x}Co_xO_2$ powders.

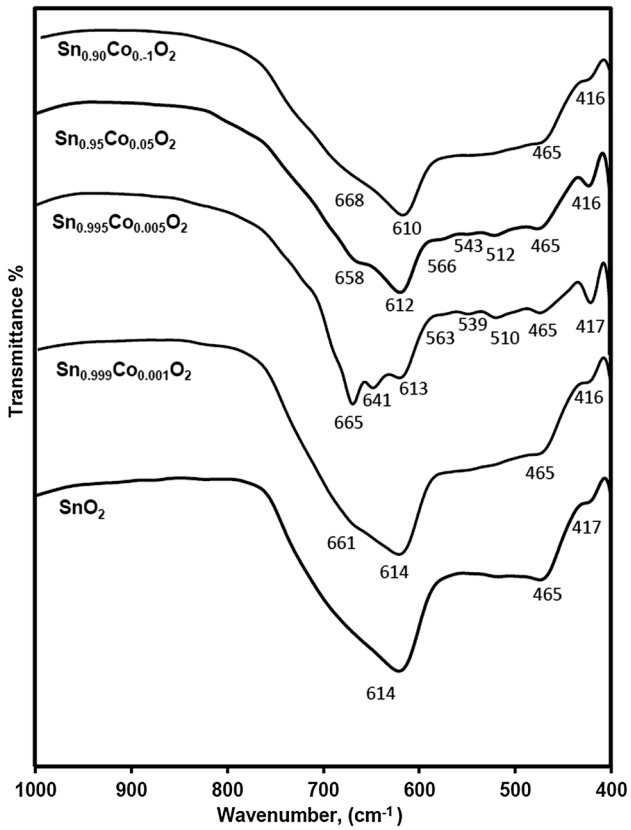

Fig. 3. FTIR spectra of $Sn_{1-x}Co_xO_2$ powders.

the variation in local defects, particle size, as well as nanoparticle morphology.[24]

Ultraviolet–Visible (UV–Vis) Absorbance Spectroscopy

UV–Vis absorption spectra as well as bandgap energy measurements of the SnO_2 and $Sn_{1-x}Co_xO_2$ samples are shown in Fig. 4. The spectra show sharp absorbance edges at 334 nm to 340 nm. The sharpness of the absorption edges is an indicator of the good crystalline nature of the prepared samples.[25] The bandgap energy (E_g) was evaluated using the equation

$$\alpha h\mu = A\left(h\mu - E_g\right)^{\frac{n}{2}}, \qquad (1)$$

where α is the absorption coefficient, h is the Planck constant, μ is the incident light frequency, E_g is the bandgap energy, and A is a constant. The value of n depends on the type of transition in the optical semiconductor[25] and takes values of 1, 3, 4, or 6 for direct allowed, direct forbidden, indirect allowed, or indirect forbidden transitions, respectively.[26]

SnO_2 exhibits a direct but dipole-forbidden transition. However, at high temperatures, direct allowed transitions are more favored in terms of absorption intensity than direct forbidden transitions.[26,27] The bandgap energy of each sample was estimated from a plot of $(\alpha h\mu)^2$ versus photon energy ($h\mu$) by extrapolating the linear part to zero absorption,[28] as shown in Fig. 4b and c. In this case, the E_g of pure SnO_2 was found to be $\sim$ 3.697 eV, in agreement with values given in literature.[29] Figure 4d shows the variation of the energy gap with the amount of Co added. Incorporation of Co^{2+} into the lattice structure of SnO_2 caused a slight increase in the E_g values ($\sim$ 3.734 eV to 3.74 eV) with respect to the undoped sample. The $Sn_{0.995}Co_{0.005}O_2$ sample showed the largest blue-shift ($E_g \sim 3.74$ eV) with respect to the other doped samples. This increase in the blue-shift cannot be explained on the basis of quantum confinement, because the latter applies for nanopowders with crystallite size smaller than 10 nm.

As in most oxide semiconductors, the top of the valence bands is derived from O 2*p* electronic states, while the bottom of the conduction bands is derived from metal Sn 5*s* electronic states.[30] The success of doping depends on the electronegativity and ionic radius of the doped and host cations.[31] The electronegativity and ionic radii of Co^{2+} are 1.88 and 72 pm, respectively, compared with 1.96 and 71 pm, respectively, for Sn^{4+}. This good matching of the electronegativity and ionic radius facilitates substitution during the preparation process,[31] as clearly shown by the XRD results.

The observed blue-shift in the bandgap can be clarified by considering the changes in the defect concentration in the doped SnO_2 as follows:

The chemical environment of surrounding oxygen anions: The formation of an oxygen vacancy releases two electrons into the system. One of these electrons fills the hole on a neighboring oxygen, while the other leads to reduction of Sn^{4+} to Sn^{2+}, which will preferably happen at surfaces and interfaces. Consequently, substitutional doping by electron donor elements such as Co^{2+} causes a variation in the chemical environment of the surrounding oxygen anions, leading to a nonstoichiometric distribution.[30]

Other donor and acceptor types: As outlined above, SnO_2 is characterized by a large fundamental bandgap of $\sim$ 3.6 eV.[26] Recent studies have shown that the conductivity of SnO_2 is not only due to the presence of defects such as oxygen vacancies (V_O) and tin interstitials (Sn_i)[29] but also the presence of donors such as hydrogen that act as unintentional donors (H_i or H_O).[29] In this case, oxygen defects may be associated with this shallow donor.[32]

However, oxygen vacancies generate donors and easily produce many electrons. On the other hand, tin vacancies are deep acceptors and will produce a negligible amount of holes in normal conditions.[33] The possible charged states of oxygen vacancies are V_O^0, V_O^+, and V_O^{++}.[34] Generally, oxygen vacancies (V_O) are the most common defects in metallic oxides and are responsible for the *n*-type conductivity in SnO_2.[34,35] This fact is due to the lower energy of formation of oxygen vacancies with respect to other defects such as tin interstitials or hydrogen

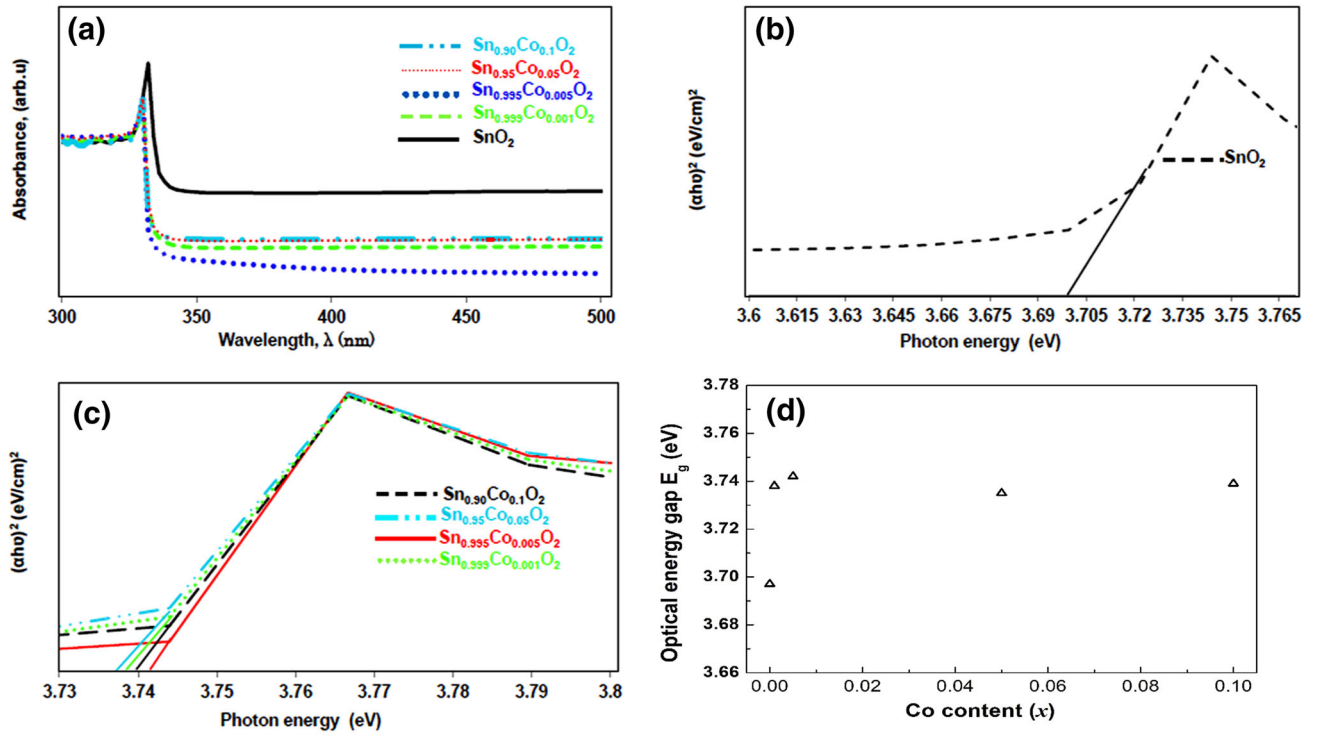

Fig. 4. (a) UV–Vis spectra of $Sn_{1-x}Co_xO_2$ powders. (b, c) $(\alpha h\mu)^2$ versus $h\mu$ for $Sn_{1-x}Co_xO_2$ powders. (d) The change of the optical energy gap with the amount of Co added in the $Sn_{1-x}Co_xO_2$ samples.

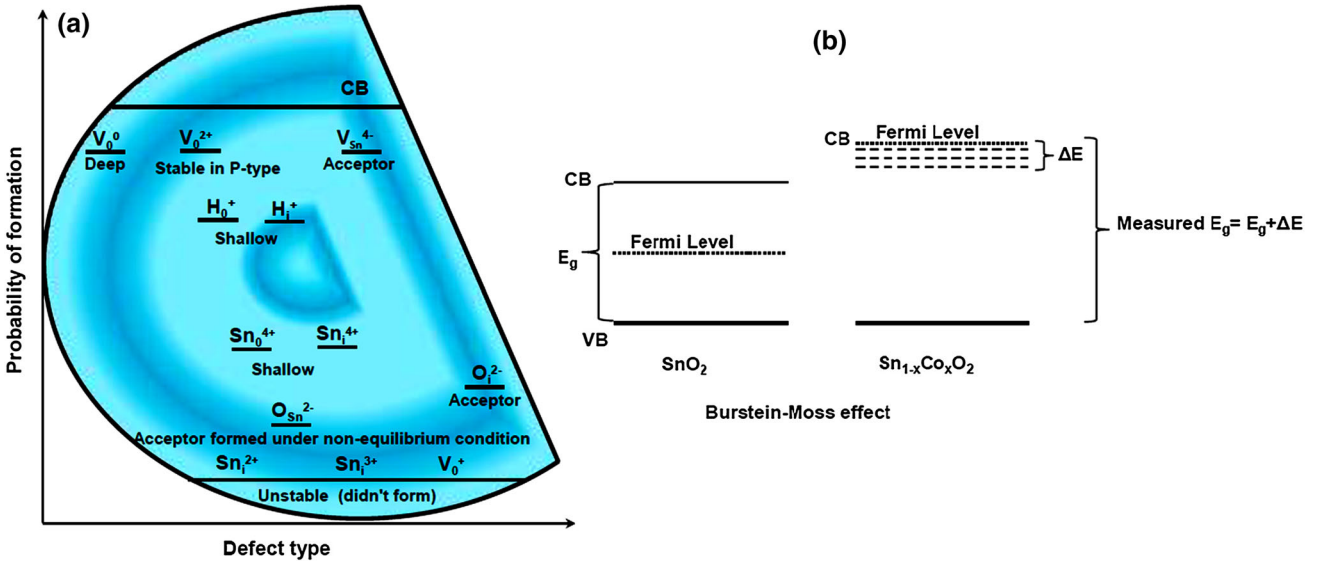

Fig. 5. (a) Probability of defect formation in $Sn_{1-x}Co_xO_2$ nanoparticles. (b) Explanation of blue-shift of optical energy gap according to Burstein–Moss effect.

defects.[35] Figure 5a shows a schematic illustration of the probability of formation of different donor and acceptor defect types in SnO_2, as an n-type semiconductor.[35–38] These probabilities are based on the energy of formation values of these defects.[34] In this case, Sn^{4+} ions are considered as acceptors which may interact with donor V_O defects present in SnO_2 to form acceptor–donor pairs.[34] These pairs create impurity levels within the energy gap and consequently decrease it.[34,39]

In this study, doping with Co^{2+} led to the creation of more V_O, as suggested by the VSM results. Such an increase in V_O leads to an increase of the bandgap energy, and a blue-shift is observed on

the basis of the Burstein–Moss effect, which originated from the lifting of the Fermi level into the conduction band due to an increase in the charge carrier concentration. In undoped *n*-type semiconductors (in this case SnO_2), the Fermi level lies nearly at the middle of the bandgap.[30] Doping with electron donors adds free electrons to the conduction band, which leads to an upwards shift of the Fermi level position to become close to the conduction-band minimum.[30] Donor electrons can enter the bottom of the conduction band.[31] According to Pauli's principle, two electrons occupying the same orbit should have different spins.[31] Therefore, the low-energy transition is suppressed and the bandgap widens, leading to the blue-shift.[31,40] Figure 5b shows the blue shift of the energy gap due to the Burstein–Moss effect, where the value of the energy gap changes according to the concentration of electrons and holes present in the different samples.[41]

Magnetic Characterization

Figure 6 shows the variation of the magnetization as a function of the applied magnetic field for the various $Sn_{1-x}Co_xO_2$ nanoparticle samples at 300 K. The *M–H* curve provides information regarding magnetic parameters such as the saturation magnetization (M_S) and coercivity (H_c), as shown in Fig. 7a and b. Ferromagnetic behavior was observed at room temperature in the undoped and doped SnO_2 samples. M_S varied in the range from 0.15 emu/g to 0.45 emu/g, and the coercive field (H_c) varied from 110 G to 200 G. M_S first increased on initial doping with Co^{2+}, then gradually decreased. Meanwhile, H_c was generally higher for the Co^{2+}-doped samples. The magnetic moment per Co^{2+} ion was calculated and is illustrated in Fig. 7c. The maximum magnetic moment per Co^{2+} ion was observed for the lowest x value, then decreased exponentially with increasing Co^{2+} concentration.

The origin of ferromagnetism (FM) at room temperature in these compounds may arise from several sources, e.g., an intrinsic property of the doped SnO_2 or the formation of some nanoscale CoO or metallic Co. However, XRD measurements revealed no secondary phases in the prepared samples. Meanwhile, the UV–Vis results suggested successful entry of Co^{2+} ions into the SnO_2 structure and modification of the bandgap. Therefore, the FM can be attributed to the intrinsic exchange interaction of magnetic moments in these compounds. The exact mechanism of intrinsic ferromagnetism in TM-doped oxides is still under debate. Although the concentration of magnetic cations is low, room-temperature FM is observed in this compound, hence direct interactions such as double-exchange or superexchange cannot be responsible for the ferromagnetism.[42] According to the donor impurity band exchange model, coupling between magnetic cations, carriers, and defects can result in bound magnetic polarons (BMPs), which may also lead to room-temperature FM. The density of oxygen vacancies may be increased because of disorder within the oxygen sublattice due to thermal processing, doping, and/or other aspects of the preparation conditions.[43] A locally trapped electron in an oxygen vacancy would have a significant effect on the spin orientation of neighboring Co^{2+} ions. According to Coey's model, the measured magnetization due to the interaction between BMPs can be described as[44,45]

$$M = M_0 L(x) + \chi_m H, \tag{2}$$

where $M_0L(x)$ accounts for the BMP contribution, where localized charge carriers strongly interact with doped ions, and $\chi_m H$ arises due to the

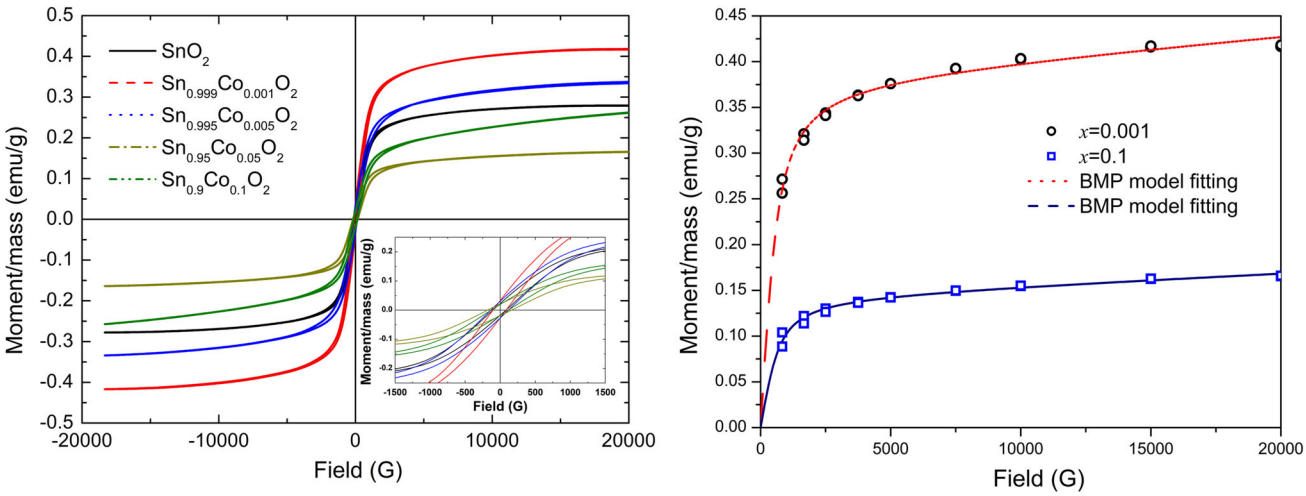

Fig. 6. Left panel: hysteresis loops for $Sn_{1-x}Co_xO_2$ samples at room temperature. The inset shows the magnified hysteresis loop, revealing clear ferromagnetic behavior. Right panel: fit according to BMP model.

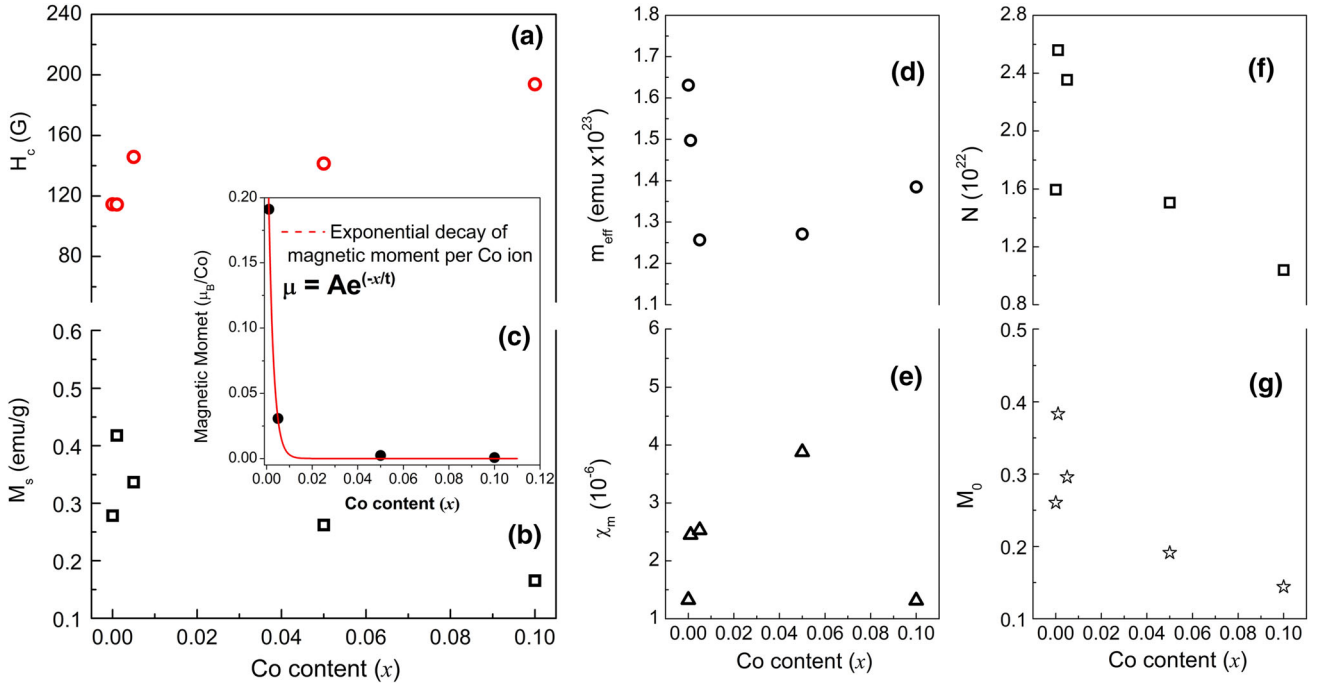

Fig. 7. (a) Saturation magnetization (M_S) and (b) coercivity (H_c) of $Sn_{1-x}Co_xO_2$ nanoparticles. (c) Magnetic moment per Co^{2+} ion as function of Co doping concentration. Fitting parameters: (d) effective magnetic moment $x = m_{eff}$, (e) paramagnetic contribution χ_m, (f) number of BMPs (N), and (g) BMP contribution M_0.

paramagnetic contribution, where the fraction of doped Co^{2+} ions which do not contribute to the BMP interaction behave paramagnetically. The spontaneous moment of the system can be written as

$$M_0 = Nm_S, \tag{3}$$

where N is the number of BMPs and m_S is the spontaneous magnetic moment of each BMP. $L(x)$ is the Langevin function,

$$L(x) = \coth(x) - \frac{1}{x}, \tag{4}$$

and x is defined as

$$x = \frac{Hm_{eff}}{K_B T}, \tag{5}$$

where $x = m_{eff}$ is an effective spontaneous magnetic moment per BMP, representing how quickly the true magnetic moment aligns with a magnetic field. At high temperatures, it can be assumed that $m_S = m_{eff}$. As indicated in the right panel of Fig. 6b, the measured experimental curves can be well fit with the BMP model. The obtained fitting parameters m_S, N, and χ_m are illustrated in Fig. 7. For all samples, the number of BMPs is on the order of $N = 10^{22}$, increasing initially with the introduction of Co^{2+} ions into the unit cell then decreasing gradually; accordingly, the BMP (M_0) contribution is expected to follow the same behavior. On the other hand, $x = m_{eff}$ generally decreases on introduction of Co^{2+} ions. This behavior would be in agreement with an exponential decrease of the magnetic moment per Co^{2+} ion. The paramagnetic susceptibility is on the order of 10^{-6} and increases with the Co^{2+} doping amount.

As stated above, oxygen vacancies are the most probable source of the FM in the studied samples, making it necessary to determine the spin nature of the vacancies. In this regard, electron spin resonance spectroscopy is a very powerful tool to differentiate types of vacancies, viz. V_O^0, V_O^+, and V_O^{++}. Only V_O^+ has unpaired electrons and hence can be detected by ESR, in contrast to the other types of vacancy.[46] The ESR spectra of the $Sn_{1-x}Co_xO_2$ nanoparticles are shown in Fig. 8, measured by lock-in phase-sensitive detection with the sample placed in a resonance cavity. The detected signal is the field derivative of the microwave absorption $dP(H)/dH$. A well-defined ESR signal which can be described by a single-derivative Lorentzian line profile was recorded for all samples.

According to Fig. 5a, V_O^+ is unstable and its formation is less probable. However, ESR measurements clearly suggested the presence of V_O^+. In fact, V_O^+ is indeed unstable, and is thought to transfer electrons to Sn^{4+} to reduce it to Sn^{2+} and thereby form the most stable V_O^{++}.[47] The detection of this unstable vacancy defect is attributed to the high resolution power of the ESR technique. The ESR parameters, viz. the integrated intensity, linewidth ΔH_{pp}, and g-factor, are summarized in Fig. 8a, b, and c, respectively. The integrated intensity is mainly proportional to the number of spins participating in the magnetic interaction. However, the

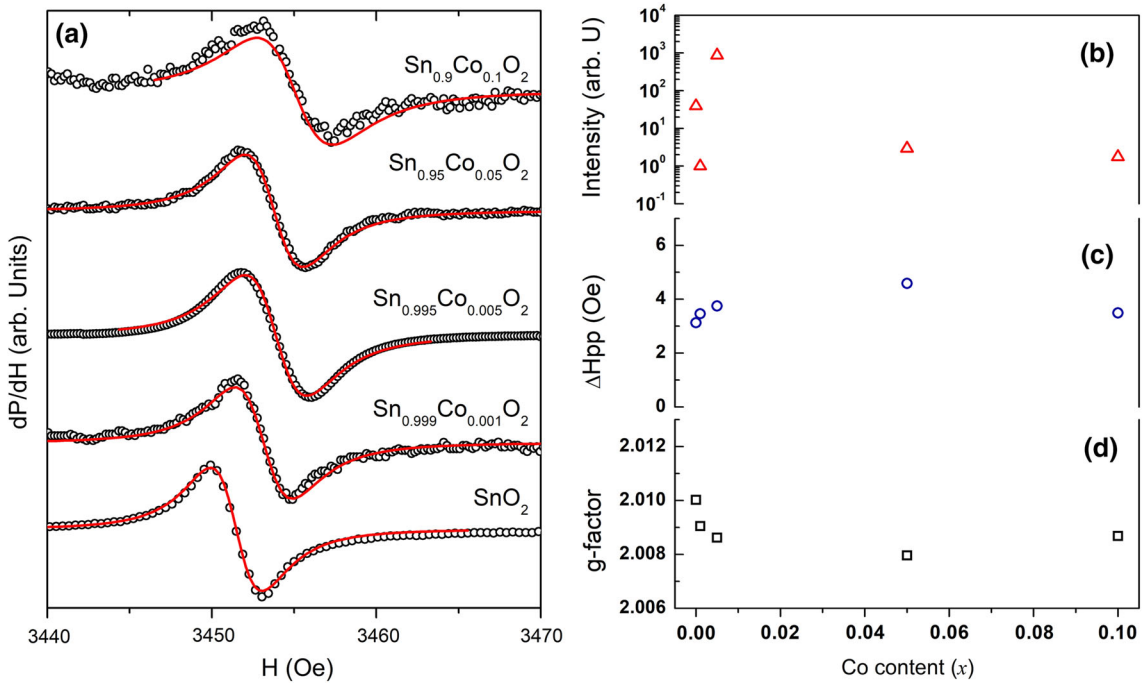

Fig. 8. (a) Room-temperature ESR spectra of different Co-doped SnO_2 nanoparticles. (b) ESR integrated intensity, (c) ESR linewidth ΔH_{pp}, and (d) *g*-factor.

localization and delocalization of the spins will also affect the spin relaxation time and thereby the ESR intensity. For less localized spins, a faster relaxation time is expected and a lower ESR intensity would be observed.[48] The highest integrated intensity was observed for the sample with $x = 0.005$, with the minimum m_{eff} and maximum bandgap energy, which may indicate greater localization of spins in this sample. The *g*-factor can be calculated from the resonance field as

$$g = \frac{h\upsilon}{\mu_B H_{res}}, \quad (6)$$

where h is the Planck constant, μ_B is the Bohr magneton, υ is the applied microwave frequency (9.71 GHz), and H_{res} is the resonance magnetic field. For all the samples, the *g*-factor ranged from 2.008 to 2.01 (Fig. 8c). The weak dependence of both the line width ΔH_{pp} and the *g*-factor confirms that the origin of the ESR signal is the same for all samples, even the undoped SnO_2, again stressing the role of trapped vacancies in the magnetic properties of these nanoparticles.

CONCLUSIONS

The preparation and structural and magnetic properties of Co^{2+}-doped SnO_2 nanoparticles were studied comprehensively. X-ray diffraction analysis confirmed the formation of single-phase tetragonal structure in all samples. Despite the low Co^{2+} content, clear morphological differences were revealed by SEM. The optical properties showed pronounced changes with the Co^{2+} doping amount. UV–Vis absorbance spectroscopy suggested that Co^{2+} doping slightly increased the bandgap energy of the studied samples. The bandgap energies E_g lay within the values expected for SnO_2. Room-temperature ferromagnetism was observed by VSM. The obtained hysteresis loops were analyzed and discussed on the basis of the bound magnetic polaron model. For all the samples, including the undoped SnO_2, the ESR signal could be well fit using a single Lorentzian line profile. Weak dependence of the linewidth ΔH_{pp} and *g*-factor was observed, suggesting that the origin of the ESR signal was the same for all samples. Among the different types of vacancy, ESR measurements illustrated that V_O^+ vacancies were responsible for the detected signal.

REFERENCES

1. S. Das and V. Jayaraman, *Prog. Mater. Sci.* 66, 112 (2014). https://doi.org/10.1016/j.pmatsci.2014.06.003.
2. T. Dietl, H. Ohno, F. Matsukura, J. Cibert, and D. Ferrand, *Science* 287, 1019 (2000).
3. A. Punnoose, K. Dodge, J.J. Beltrán, K.M. Reddy, N. Franco, J. Chess, J. Eixenberger, and C.A. Barrero, *J. Appl. Phys.* 115, 17B534 (2014).
4. S. Ferrari, L.G. Pampillo, and F.D. Saccone, *Mater. Chem. Phys.* 177, 206 (2016).
5. R.K. Zulfiqar, Y. Yuan, Z. Iqbal, J. Yang, W. Wang, Z. Ye, and J. Lu, *J. Mater. Sci. Mater. Electron.* 28, 4625 (2017).
6. Y. Li, W. Yin, R. Deng, R. Chen, J. Chen, Q. Yan, B. Yao, H. Sun, S.H. Wei, and T. Wu, *NPG Asia Mater.* 4, 1 (2012).
7. R. Pushpa, P. Kumar, B. Ramanujam, and A. Punnoose, *J. Magn. Magn. Mater.* 407, 46 (2016).
8. R. Adhikari, A.K. Das, D. Karmakar, T.V. Chandrasekhar Rao, and J. Ghatak, *Phys. Rev. B* 78, 024404 (2008).

9. M. Ghalkhani, B. Hosseininia, J. Beheshtian, and A.A. Firooz, *J. Mater. Sci. Mater. Electron.* 28, 7568 (2017). https://doi.org/10.1007/s10854-017-6448-y.
10. M.S. Pereira, T.S. Ribeiro, F.A.S. Lima, L.P.M. Santos, C.B. Silva, P.T.C. Freire, and I.F. Vasconcelos, *J. Nanopart. Res.* 20, 212 (2018).
11. C. Zhang and J. Lin, *Chem. Soc. Rev.* 41, 7938 (2012).
12. L.M. Fang, X.T. Zu, Z.J. Li, S. Zhu, C.M. Liu, L.M. Wang, and F. Gao, *J. Mater. Sci. Mater. Electron.* 19, 868 (2008).
13. M.P. Rajeeva, C.S. Naveen, A.R. Lamani, and H.S. Jayanna, *J. Mater. Sci. Mater. Electron.* 28, 16348 (2017). https://doi.org/10.1007/s10854-017-7542-x.
14. A.S. Ahmed, S.M. Muhamed, M.L. Singla, S. Tabassum, A.H. Naqvi, and A. Azam, *J. Lumin.* 131, 1 (2011). https://doi.org/10.1016/j.jlumin.2010.07.017.
15. M. Garcia-Tecedor, D. Maestre, A. Cremades, and J. Piqueras, *J. Phys. Chem. C* 120, 22028 (2016).
16. B. Cojocaru, D. Avram, V. Kessler, V. Parvulescu, G. Seisenbaeva, and C. Tiseanu, *Sci. Rep.* 7, 9598 (2017).
17. M. Yehia, Sh. Labib, and S.M. Ismail, *Phys. B Condens. Matter* 446, 49 (2014).
18. M. Bortolotti, L. Lutterotti, and I. Lonardelli, *J. Appl. Cryst.* 42, 538 (2009).
19. J. Gajendiran and V. Rajendran, *Optoelectron. Adv. Mater.* 5, 44 (2011).
20. R. Yogamalar, V. Mahendran, R. Srinivasan, A. Beitollahi, R.P. Kumar, A. Chandra Bose, and A. Vinutures, *Chem. Asian J.* 5, 2379 (2010).
21. R. Hu, Y. Ouyang, T. Liang, H. Wang, J. Liu, J. Chen, C. Yang, L. Yang, and M. Zhu, *Adv. Mater.* 29, 1605006 (2017).
22. M. Faisal, A.A. Ibrahim, F.A. Harraz, H. Bouzid, M.S. Al-Assiri, and A.A. Ismail, *J. Mol. Catal. A Chem.* 397, 19 (2015).
23. A.M. Ungureanu, O. Oprea, B.S. Vasile, C. Andronescu, G. Voicu, I. Jitaru, and T. Cent, *Eur. J. Chem.* 12, 909 (2014). https://doi.org/10.2478/s11532-013-0400-7.
24. S.A. Saleh, A.A. Ibrahim, and S.H. Mohamed, *Acta Phys. Pol. A* 129, 1220 (2016).
25. Sh. Labib, *J. Saudi Chem. Soc.* 21, 664 (2017).
26. J. Jiang, Y. Lu, B.K. Meyer, D.M. Hofmann, and M. Eickhoff, *J. Appl. Phys.* 119, 245703 (2016).
27. M. Weidner, *Fermi Level Determination in Tin Oxide by Photoelectron Spectroscopy: Relation to Optoelectronic Properties; Band Bending at Surfaces and Interfaces; Modulation Doping*, Ph.D. Thesis to TU Darmstadt (2015).
28. A. Abdelkrim, S. Rahmane, O. Abdelouahab, N. Abdelmalek, and G. Brahim, *Optik* 127, 2653 (2016).
29. A.M. Ganose and D.O. Scanlon, *J. Mater. Chem. C* 4, 1467 (2016).
30. X. Yu-Jing, G. Zi-Sheng, and H. Tao, *Chin. Phys. B* 23, 087701 (2014).
31. T.B. Ivetić, M.R. Dimitrievska, N.L. Finčur, Lj.R. Dačanin, I.O. Gśth, B.F. Abramović, and S.R. Lukić-Petrović, *Ceram. Int.* 40, 1545 (2014).
32. H. Wafula, A. Juma, T. Sakwa, R. Musembi, and J. Simiyu, *Coatings* 6, 30 (2016).
33. S.S. Kim, H.G. Na, H.W. Kim, V. Kulishand, and P. Wu, *Sci. Rep.* 5, 10723 (2015).
34. X. Li, R. Deng, Y. Li, B. Yao, Z. Ding, J. Qin, and Q. Liang, *Ceram. Int.* 42, 5299 (2016).
35. A. Janotti, J.B. Varley, J.L. Lyons, and C.G. Van de Walle, *Controlling the Conductivity in Oxide Semiconductors*, ed. J. Wu, J. Cao, W.-Q. Han, A. Janotti, and H.C. Kim (Berlin: Springer, 2012), p. 23.
36. A.K. Singh, A. Janotti, M. Scheffler, and C.G. Van de Walle, *Phys. Rev. Lett.* 101, 055502 (2008).
37. V.B. Kamble and A.M. Umarji, *AIP Adv.* 3, 082120 (2013).
38. D.B. Granato, J.A. Caraveo-Frescas, H.N. Alshareef, and U. Schwingenschl Ögl, *Appl. Phys. Lett.* 102, 212105 (2013).
39. R. Singh, M. Kumar, S. Shankar, R. Singh, A.K. Ghosh, O.P. Thakur, and B. Das, *Mater. Sci. Semicond. Process.* 31, 310 (2015).
40. E. Mokaripoor and M.-M. Bagheri-Mohagheghi, *Mater. Sci. Semicond. Process.* 30, 400 (2015).
41. J.J.J. Carey, M. Legesse, and M. Nolan, *J. Phys. Chem. C* 120, 19160 (2016).
42. B. Pal and P.K. Giri, *J. Nanosci. Nanotechnol.* 11, 9167 (2011).
43. E. Swatsitang, S. Phokha, S. Hunpratub, and S. Maensiri, *Phys. B Condens. Matter* 485, 14 (2016).
44. T. Debnath, S. Das, D. Das, and S. Sutradhar, *J. Alloys Compd.* 696, 670 (2017).
45. A. Bandyopadhyay, S. Sutradhar, B.J. Sarkar, A.K. Deb, and P.K. Chakrabarti, *Appl. Phys. Lett.* 100, 252411 (2012). https://doi.org/10.1063/1.4729386.
46. S. Shi, D. Gao, X. Qiang, Z. Yang, and D. Xue, *RSC Adv.* 4, 45467 (2014).
47. K.G. Godinho, A. Walsh, and G.W. Watson, *J. Phys. Chem. C* 113, 439 (2009). https://doi.org/10.1021/jp807753t.
48. A. Möller, T. Taetz, N. Hollmann, J.A. Mydosh, V. Kataev, M. Yehia, E. Vavilova, and B. Büchner, *Phys. Rev. B* 76, 134411 (2007).